834 Biophysical Journal Volume 91 August 2006 834–841

Mechanical Deformation of Spherical Viruses with Icosahedral Symmetry

Gerard Adriaan Vliegenthart and Gerhard Gompper
Institut für Festkörperforschung, Forschungszentrum Jülich, Jülich, Germany

ABSTRACT Virus capsids and crystalline surfactant vesicles are two examples of self-assembled shells in the nano- to micrometer size range. Virus capsids are particularly interesting since they have to sustain large internal pressures while encapsulating and protecting the viral DNA. We therefore study the mechanical properties of crystalline shells of icosahedral symmetry on a substrate under a uniaxial applied force by computer simulations. We predict the elastic response for small deformations, and the buckling transitions at large deformations. Both are found to depend strongly on the number of elementary building blocks N (the capsomers in the case of viral shells), the Föppl-von Kármán number γ (which characterizes the relative importance of shear and bending elasticity), and the confining geometry. In particular, we show that whereas large shells are well described by continuum elasticity-theory, small shells of the size of typical viral capsids behave differently already for small deformations. Our results are essential to extract quantitative information about the elastic properties of viruses and vesicles from deformation experiments.

INTRODUCTION

The formation of regular polyhedra is a frequently encountered strategy of nature to optimize self-assembled structures. Microscopic boron clusters (1), mesoscopic surfactant vesicles (2), vesicles formed from wheel-shaped molybdenum clusters (3), as well as about half of all known spherical virus particles (4) are all small self-assembled structures that have an underlying icosahedral symmetry. It is interesting that the overall three-dimensional structure of many viruses is so similar whereas they are built from different protein subunits. Two illustrative examples of well-known viruses are the tomato bushy stunt virus and the bacteriophage ϕ29. Tomato bushy stunt virus was the first virus for which the icosahedral structure was predicted (5) and later confirmed by virus crystallography (6). This virus consists of 180 protein subunits that aggregate into a virus shell of ~34-nm diameter that encapsulates the viral genome. The typical contact energy between the different subunits is in the range of 100–400 kJ/mol, which corresponds to several tens of k_BT per bond. The bacteriophage ϕ29 is a small bacteria-infecting virus consisting of a head of 235 gp8 protein subunits—forming two icosahedral end caps and a cylindrical equatorial region—and a long flexible tail (7). It has been demonstrated by DNA packaging experiments using optical tweezers (8) that the genome of this virus is very tightly packed into the capsid by a molecular motor, leading to an internal pressure of ~50 atm (9). This high pressure results in a formidable injection force when the virus infects a host cell. Therefore, virus capsids must be mechanically very strong.

Different types of protein subunits aggregate under the appropriate conditions (ionic strength, pH, temperature) into stable virus capsids. However, the mechanically coherent shell often consists of only a single kind of protein subunit. This process of spontaneous aggregation is very similar to micellization in surfactant solutions and can be largely understood using self-assembly theory (10–12). Recently, several groups studied the formation of these icosahedral particles by computer simulation (13–15). More complex shapes can be obtained by introducing a spontaneous curvature that competes with the ratio of bending and stretching energy (13,16). The origin of the stability of the icosahedral shape as an approximation to a sphere lies in the fact that any regular triangulation of a smooth sphere requires an excess of at least 12 fivefold disclinations (17). Caspar and Klug (18) first showed that the organization of proteins in the viral shell is such that a few proteins each form hexavalent and pentavalent morphological units, the capsomers. Furthermore, the icosadeltahedral structure of a virus shell can then be characterized by two integers p and q such that the number of vertices (i.e., of the morphological units) is $N = 10T + 2$, the number of triangles is $N_T = 20T$, and the number of subunits is $N_S = 3N_T$, where $T = p^2 + pq + q^2$, the so-called T-number of the virus. For many virus particles, relatively few subunits are involved so that T and N_T are small.

Given the intrinsic strength of the virus capsids that follows from experiments (8) as well as from calculations of protein-protein interactions (19), it is important to probe the mechanical properties of viruses directly by means of single-particle experiments. The main question is then how to relate the experimentally accessible observable to the elastic constants of the virus capsid. Recently, controlled experiments using scanning-force microscopy have been used to measure the mechanical properties of (empty) bacteriophage ϕ29 capsids (20). Similar measurements on hollow spherical

---

Submitted January 17, 2006, and accepted for publication April 26, 2006.

Address reprint requests to G. A. Vliegenthart, Institut für Festkörperforschung, Forschungszentrum Jülich, D-52425 Jülich, Germany. Tel.: 0049-2461-616131; Fax: 0049-2461-612850; E-mail: g.vliegenthart@fz-juelich.de.

0006-3495/06/08/834/08 $2.00

doi: 10.1529/biophysj.106.081422

polyelectrolyte capsules (21) were reported in Lulevich et al. (22) and Fery et al. (23).

In this article, we investigate how the elastic parameters, the size of the shell, and the confining geometry lead to particular mechanical responses, and reveal the underlying deformation pathways. Furthermore, we show how the elastic constants can be extracted from deformation experiments in combination with the relaxed shape of the virus. Therefore, we performed molecular dynamics computer simulations on shells of icosahedral symmetry, which were modeled as triangulated surfaces with well-defined elastic properties. In a coarse-grained description, the elastic deformation energy of the shell has two contributions, the in-plane stretching energy and the bending energy. Triangulated surfaces with a small number of vertices resemble virus particles (14) if a triangular facet is identified with three protein subunits (as suggested by Caspar and Klug (18)), whereas triangulated surfaces with a large number of vertices (24) are highly simplified models for large viruses and spherical surfactant vesicles with crystalline order.

MODEL

Triangulated surfaces

We performed molecular dynamics computer simulations on triangulated icosahedral vesicles with stretching and bending energy. Such a vesicle is created by starting from a perfect icosahedron. A planar hexagonal network with an adjustable lattice constant is attached to one of its faces, such that the three corners of the icosahedron coincide with three lattice points. The number of steps p from one corner along one row of nearest-neighbor bonds, followed by q steps after a 60° rotation to reach another corner defines the pair of integers in the Caspar-and-Klug classification. The other faces are decorated accordingly, such that the lattice orientations of neighboring faces match perfectly. This procedure generates vesicles of T-numbers $\{1, 3, 4, 7, 9, \ldots.\}$. The vertices in this network correspond to the viral capsomers. In our model, the vertices are connected irreversibly by harmonic springs, which implies the stretching energy,

$$V_s = \frac{k}{2}\sum_{\langle i,j\rangle}(|\mathbf{r}_i - \mathbf{r}_j| - r_0)^2, \tag{1}$$

with equilibrium distance r_0 and spring constant k, which determines the two-dimensional Young modulus $K_0 = 2k/\sqrt{3}$ (25). The sum in Eq. 1 runs over all bonds that connect the nearest-neighbor pairs of vertices i and j. The bending energy,

$$V_b = \lambda \sum_{\alpha,\beta}(1 - \mathbf{n}_\alpha \cdot \mathbf{n}_\beta), \tag{2}$$

is determined by the scalar product of the normal vectors of adjacent triangles, two of which are indicated by the black arrows in Fig. 1 *B*. The bending rigidity κ is related to the elastic constant λ via $\kappa = \sqrt{3}\lambda/2$. The sum runs over all pairs of triangles.

The balance between the stretching and bending energies is characterized by the dimensionless Föppl-von Kármán number $\gamma = K_0R_v^2/\kappa$, where R_v is the (average) radius of the virus in the relaxed state. It has been shown that γ determines the equilibrium shape of icosahedral vesicles with zero spontaneous curvature (24,26,27). To be more precise, for $\gamma < 130$ a fivefold disclination is stable in a locally flat environment and vesicles are dominated by rounded shapes, whereas for larger values of γ the disclination becomes unstable and induces buckling of the surface, resulting in a faceted vesicle with smooth ridges. With further increasing γ, the ridges become sharper and enter an asymptotic regime characterized by universal power laws for $\gamma > 10^7$. Moreover, Lidmar et al. (24) demonstrated by comparing numerical results and data of virus shapes for bacteriophage HK97 and the yeast L-A virus that for viruses the Föppl-von Kármán number is typically in the range $100 < \gamma < 2000$.

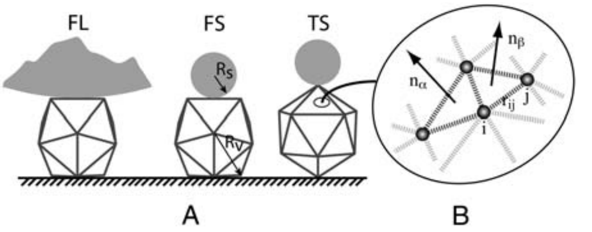

FIGURE 1 Icosahedron of radius R_v confined between a sphere of radius R_s and a plate. (*A*) A vesicle lying on one of its faces and compressed by a large sphere (*left*), a vesicle lying on one of its faces and compressed by a small sphere (*middle*), and a vesicle standing on one of its tips and compressed by a small sphere (*right*). (*B*) Detail of triangulated surface with local normal vectors $\mathbf{n}_\alpha$ and $\mathbf{n}_\beta$ and harmonic springs indicated by gray dashed lines.

Mechanical deformation

In the simulations, a deformation experiment is carried out as follows. A vesicle of radius R_v in the relaxed state is confined between a planar substrate and a sphere of radius R_s. This sphere should be compared to a sphere on the tip of an atomic force microscope. The substrate is fixed while the sphere moves downward (in the z-direction) at a constant rate. This mimics the standard procedure employed in single-molecule experiments, e.g., on stretching DNA (28) or compressing viruses (20). When the sphere moves downward, the vesicle deforms to fit in the remaining space. The elastic force of the vesicle can be measured directly from the force on the sphere in the z-direction.

The interaction between the vertices of the vesicle and the confining sphere or the bottom plate is described by a Lennard-Jones potential which is truncated at its minimum and shifted. Since we focus on the purely elastic effects, plasticity and fracture are not taken into account. Furthermore, for the range of compressions up to 50%, different parts of the shell do not touch; therefore, self-avoidance effects are not relevant and are not taken into account.

The simulations were performed by using molecular dynamics, including noise and friction terms, in the underdamped regime. We employ a velocity Verlet implementation of the algorithm described in van Gunsteren and Berendsen (29). In addition, velocities were rescaled periodically. This molecular dynamics scheme guarantees that under the applied external force the temperature remains constant and that angular momentum is zero on average. We chose a temperature such that $\kappa/k_BT \geq 10^2$ and $K_0r_0^2/k_BT \geq 10^3$, so that the mechanical energy dominates over thermal contributions.

The vesicles were compressed at a constant rate to ~50% of their original size. We chose a compression rate small enough that the energies and forces involved were essentially independent of it. This can be estimated by comparing the thermal velocity, $v_{th} = \sqrt{3k_BT/m}$, of the vertices and the transverse sound velocity, $c_s = \sqrt{\mu/\rho}$ (where $\mu = \sqrt{3}k/4$ is the shear modulus, $\rho = 2m/\sqrt{3}r_0^2$ is the mass density, and m is the mass of a single membrane vertex), with the compression velocity v_{comp}. Since for all values of the spring constants in our simulations, $c_s \gg v_{th}$, we use the thermal velocity to estimate $v_{comp}/v_{th} \approx 0.015$. Thus, the deformations propagate almost instantaneously through the material. On the other hand, the compression is fast enough that thermal fluctuations play a minor role in assisting buckling transitions.

Simulations were usually performed for the three geometries illustrated in Fig. 1 *A*, a vesicle lying on a face deformed by a large sphere with $R_s = 50R_v$, indicated by FL; a vesicle lying on a face deformed by a small sphere with $R_s = 3r_0$, denoted by FS; and a vesicle standing on a tip deformed by a small sphere with $R_s = 3r_0$, indicated by TS. The calculations were done for triangulation (*T*) numbers $1 \leq T \leq 1024$, with elastic constants such that $10^{-1} < \gamma < 10^6$. Therefore, the whole range from the spherical ($\gamma < 130$) to the asymptotic "stretching-ridge" ($\gamma > 10^7$) regime was covered.

In all simulations, the total force parallel to the substrate was set to zero to prevent the vesicles from jumping out sideways. Furthermore, to prevent the tip-standing vesicle (TS) from falling over, we fixed the location of both the vertex on which the vesicle was standing and the top vertex on the line along which the force is applied. For the vesicles lying on a face initially, we observe a rotation for sufficiently large deformations. Whereas for a compression with a large sphere such a behavior should be observable experimentally (in particular if a soft potential is employed in addition to constrain the horizontal motion of the vesicle), it is certainly unrealistic for compression with a small sphere. Therefore, in both the FS and FL geometries, we also investigated the case where the vesicle is glued to the substrate with its bottom face.

RESULTS

Relaxed virus shapes

Let us first consider the energy of vesicles in the absence of an external force. In the continuum limit and for $\gamma < 10^4$, this energy is approximated very well by (24)

$$\frac{E}{\kappa} \simeq \begin{cases} 6B\gamma/\gamma_b + D & \gamma < \gamma_b \\ 6B[1 + \ln(\gamma/\gamma_b)] + D & \gamma > \gamma_b \end{cases}, \tag{3}$$

with $B \simeq \pi/3$ and $D = 8\pi/3$, and where $\gamma_b \approx 130$ locates the transition between spherical and weakly faceted vesicles. In Fig. 2, we show the energy as a function of vesicle size for three γ-values. To obtain the elastic energy without thermal contributions, the simulated shapes were cooled to zero temperature in this case.

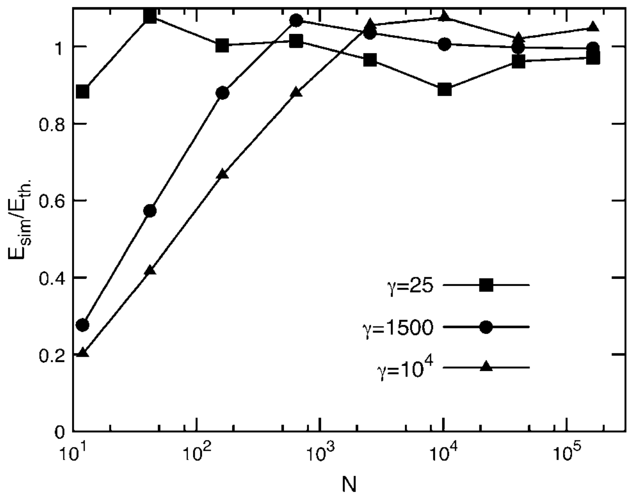

FIGURE 2 Ratio of the elastic energy of a vesicle from simulations and the theoretical prediction (see Eq. 3) as a function of the vesicle size and for three γ-values.

For small γ, the energy converges rapidly to the continuum limit, whereas for large γ, substantially larger networks are required. This indicates that for small γ-values, continuum theory can be applied with sufficient accuracy even to relatively small viruses, whereas for larger viruses and vesicles, finite-size effects become important.

Force-compression relations

Next we investigate the elastic response of vesicles for a broad range of elastic parameters and vesicle sizes. Force-compression curves were calculated varying either the vesicle size, the size of the compressing sphere, or γ. The results can be classified in two ''families'' of qualitatively different force-compression dependencies, as illustrated in Fig. 3 for two γ values in the FL-geometry. For a small Föppl-von Kármán number, $\gamma = 50$, the force-compression data for

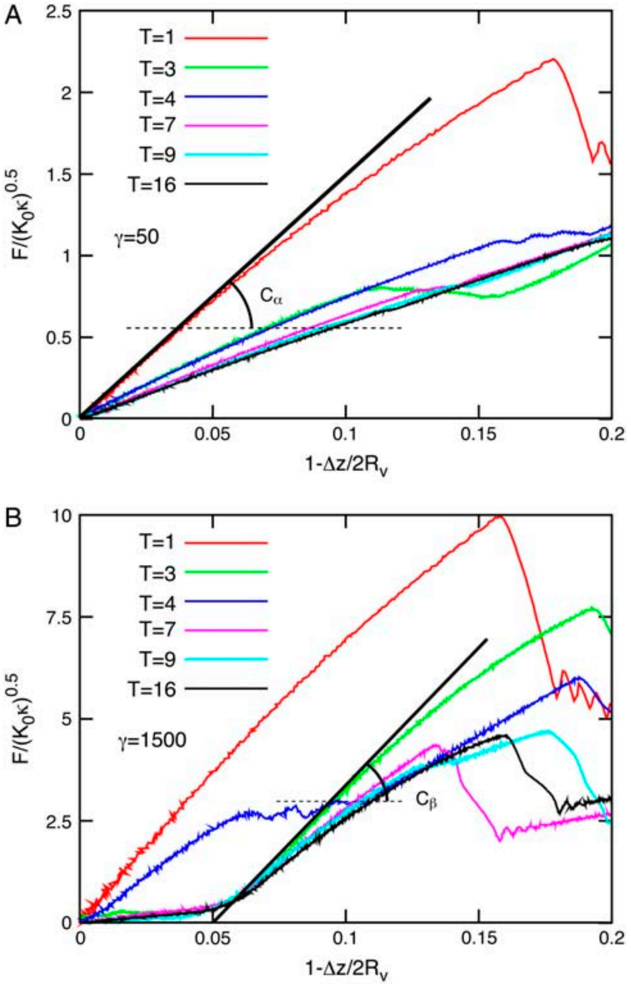

FIGURE 3 Force-compression curves for a vesicle on its face compressed with a large sphere (FL). Data are presented for six different vesicle sizes with (*A*) $\gamma = 50$ and (*B*) $\gamma = 1500$. The solid line in *A* indicates the linear force-compression relation given by Eq. 4 with $C_\alpha = 5$; the solid line in *B* represents the same relation with $C_\beta = 19.4$.

different vesicle sizes quickly converge with increasing T-number or N to an almost linear master curve—after scaling the compression with R_v and the force with $\sqrt{K_0\kappa}$. This limiting behavior is achieved for $T > 5$. In the case of a larger Föppl-von Kármán number, $\gamma = 1500$, the data are characterized by discontinuous jumps at larger compressions. These jumps correspond to buckling events; a sudden rearrangement in the vesicle results in an almost instantaneous decrease of the force on the sphere.

The linear force-compression curves for small γ (Fig. 3 *A*) can be well described by the universal Hookean scaling relation,

$$\frac{FR_v}{\kappa\sqrt{\gamma}} = C\left(1 - \frac{\Delta z}{2R_v}\right), \tag{4}$$

where F is the force the vesicle exerts on the sphere and $\Delta z = z_{\text{sphere}} - z_{\text{plate}} - R_s$ is the vertical deformation. The scaling factor, $R_v/\kappa\sqrt{\gamma} = 1/\sqrt{K_0\kappa}$, is the same as was found for the scaling of the buckling force of spherical shells (30) and of stretching ridges in thin elastic sheets (31,32). For large γ, the initial slope of the buckling curve can be described by the same scaling relation (i.e., with the same value of C), whereas for larger compressions a second linear regime is observed with a different (larger) effective spring constant (compare Fig. 3 *B*). The origin of these two regimes in the FL geometry is that first the confining sphere touches and deforms the top face of the icosahedron; then, when the deformation is large enough that the sphere touches the three top corners of the icosahedron, the vertical ridges start to be deformed, which requires a larger force.

To distinguish the two linear regimes, we denote the prefactor in Eq. 4 by C_α for the initial compression and C_β for the more advanced compression. In Fig. 4, we show force-compression curves for a range of radii of the compressing sphere and as a function of γ. From the data in Fig. 4, we find that C_α is a function of R_s/R_v alone, whereas C_β is a function of both R_s/R_v and γ. Both curves saturate in the limit of large R_s/R_v, which corresponds to the compression of a virus particle between two planar walls. The prefactors C_α and C_β are increasing functions of R_s/R_v, since the confinement becomes more severe at larger R_s. For increasing sphere radius the scaled buckling force increases, since the vertical ridges are progressively more involved in the deformation process. Moreover, the buckling compression shifts to lower values as the deformation changes from local for small spheres to global for large spheres.

Our results for C_α for large N should be compared with $C_\alpha = 7.35$, derived in Ivanovska et al. (20), for an elastic sphere compressed by equal and opposite point forces applied at the poles. We find in the FL geometry for both $\gamma = 50$ and $\gamma = 1500$ that $C_\alpha \approx 5$ (Fig. 3); for $\gamma = 7700$, C_α increases from 3.5 for small R_s/R_v to 6.2 for large R_s/R_v (Fig. 4).

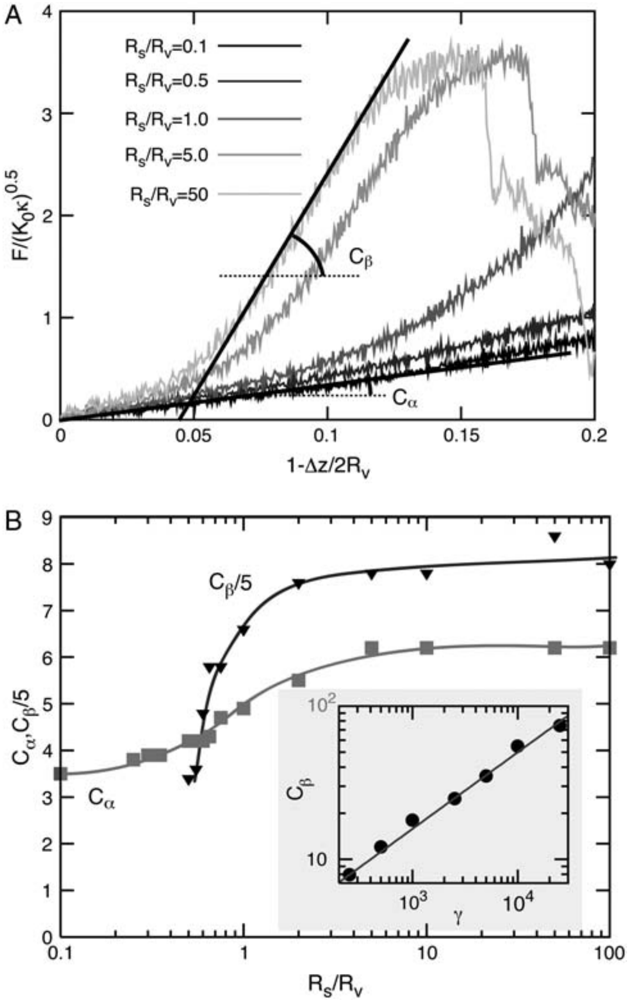

FIGURE 4 Force-compression curves for a vesicle on its face. (*A*) Compression by spheres of different sizes for $\gamma = 7700$ and $N = 642$. (*B*) Dependence of C_α and C_β on the size ratio R_s/R_v for $\gamma = 7700$ and $N = 642$. (*Inset*) The γ-dependence of C_β for $R_s/R_v = 50$ and $N = 2562$.

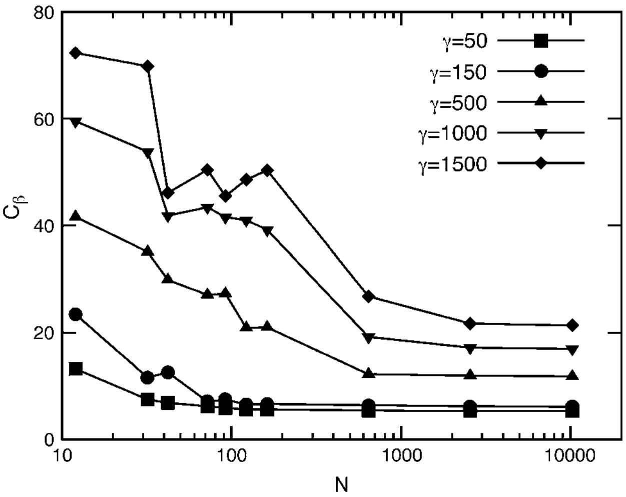

FIGURE 5 Effective spring constant C_β in the FL geometry as a function of the number of vertices N for different values of the Föppl-von Kármán number γ.

Our model treats the shell as a two-dimensional mathematical surface. This neglects the local deformation of the protein layer (Hertz contact) (20). The Hertz model for the elastic deformation of solid homogeneous bodies predicts the measured force on the cantilever tip to scales like $F \sim \Delta z^{2/3}$ (30,33). Such a behavior is expected for very small indentations on the scale of the thickness of the protein layer, before the linear dependence due to shell deformation sets in.

Finite-size effects

It is already evident from Fig. 3 that the force-compression relations for small N and large γ display pronounced finite-size effects. This is important for the investigation of viruses, which fall mostly into the range of small T-numbers. The dependence of the effective spring constant C_β on the vesicle size N, shown in Fig. 5, demonstrates that finite-size effects become more important with increasing γ. For large N, all curves reach a plateau, which we identify as the continuum limit. Typically, small vesicles are apparently less flexible than predicted by continuum theory, which results in a larger force at the same compression for small N. It is important to take these effects into account when elastic parameters are to be extracted from force-compression experiments of small viral capsids.

Buckling

We have analyzed the data from our force-compression curves further by measuring both the buckling force and the buckling compression as a function of γ. Here the buckling force for a given system is defined as the smallest force for which a buckling event is found. Similarly, the buckling compression is defined as the compression at which buckling first occurs.

The results are presented in Fig. 6 for all three geometries. The scaled buckling force, shown in Fig. 6 *A*, is found to

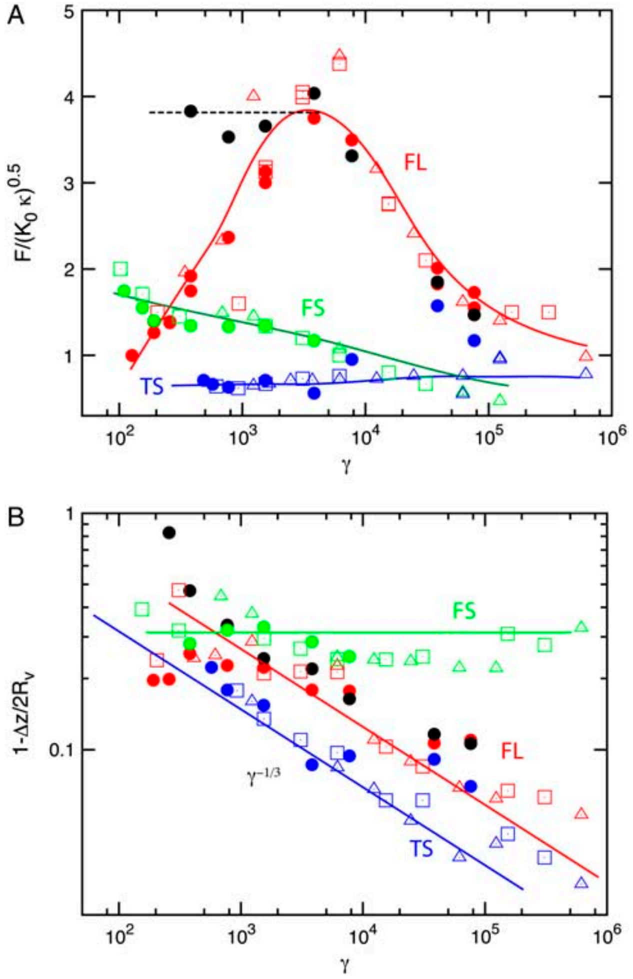

FIGURE 6 Buckling of virus under compression in three different geometries. (*A*) Scaled buckling force and (*B*) buckling compression as a function of the Föppl-von Kármán number γ. Red symbols indicate results for the FL geometry, green symbols for the FS geometry, and blue symbols for the TS geometry. Shown are results for $N = 642$ (●), $N = 2562$ (□), and $N = 10242$ (△). The solid black circles indicate simulations for a shell that was glued to the substrate. Solid lines are guides to the eye. The red and blue lines in *B* indicate scaling with $\gamma^{-1/3}$.

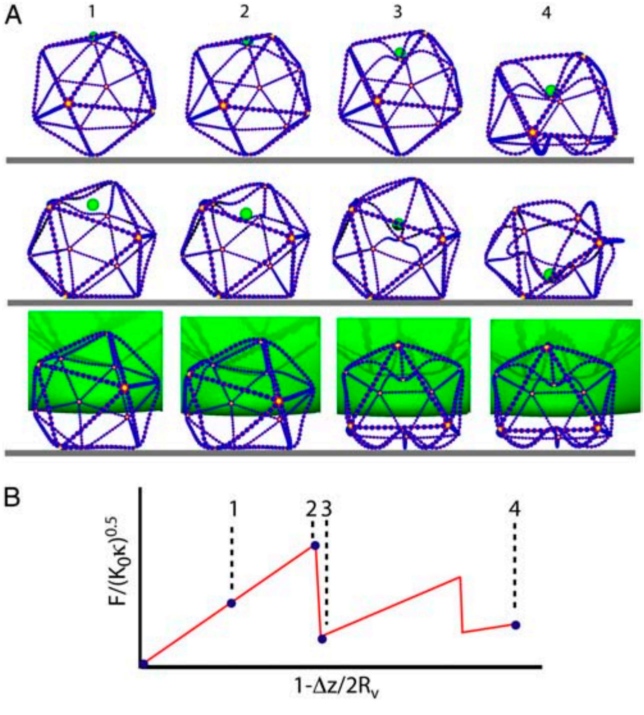

FIGURE 7 Sequence of configurations for $N = 2562$ and $\gamma = 1500$. The top row is for the TS, the middle row for the FS, and the bottom row for the FL geometry. For clarity, instead of the full virus surface, only the lines connecting the fivefold coordinated vertices (*yellow*) are shown. The green sphere exerts the external force, the blue spheres connect the fivefold coordinated vertices. The substrate (support) is indicated by the gray line and the images are taken slightly from below. The images of each row show configurations (*1*) at a moderate compression, (*2*) at the maximum force of the first buckling event, (*3*) at the force minimum just after buckling, and (*4*) at the final state of 50% compression.

depend very weakly on γ. This indicates that the buckling force is essentially proportional to $\sqrt{K_0\kappa}$ over the whole γ-range, in agreement with results for spherical shells (30) and stretching ridges (31). However, qualitative and quantitative differences between the different compression geometries can clearly be seen in Fig. 6 *A*, in particular a pronounced maximum in the FL geometry. The qualitative different behaviors in the different compression geometries appear even more pronounced in the buckling compression, see Fig. 6 *B*. Although the buckling compression in the FS geometry is nearly independent of γ, for the TS and FL geometries a distinct reduction of the buckling compression with increasing γ is observed, which follows roughly a $(1 - \Delta z/2R_v) \sim \gamma^{-1/3}$ power-law dependence. The latter scaling behavior has been predicted for the buckling transition of stretching ridges in thin elastic sheets for a compressive force along the ridge direction (31,32). We believe that the reason such a power-law behavior is not seen in the FS geometry is that the force is mainly perpendicular to the ridge direction in this case. The scatter in the data presented in Fig. 6 is due to the fact that we performed the calculations for different combinations of K_0 and κ. The standard deviation of the data for a single parameter set is $<2\%$.

The geometry dependence of the buckling pathways was analyzed by considering the local rearrangements, as well as by the global reorientation of the vesicles during deformation. For vesicles standing on the tip (the TS geometry), the scaled buckling force is virtually independent of γ, as shown in Fig. 6 *A*. The buckling event for this geometry is illustrated by the sequence of images in the top row of Fig. 7. The fivefold rotational symmetry of the shape with respect to the force axis is approximately preserved during the whole deformation process—with larger deviations for large γ. The overall deformation associated with the first buckling event is rather small. The top tip folds in only partially (compare Fig. 7). The final state involves buckling of the lower tip also, so that the top-down symmetry is restored. Further compression leads to deformation of the ''vertical'' faces and involves a large force. For $\gamma > 10^5$, the characteristic large jumps in the buckling curves disappear. Instead, the data look very noisy. The origin for this behavior is that the vesicle crumples—as happens when an icosahedron made of paper is subjected to a point force at its tip. The ''noise'', therefore, corresponds to a large number of small buckling events.

In the case of the vesicle lying on the face compressed by a small sphere (the FS geometry; see Fig. 7, *middle row*), the top face of the icosahedron is deformed as long as the compression is small. At some point one of the top corners buckles in, accompanied by a rotation of the vesicle and buckling of the diagonally opposite bottom corner (not shown). The buckling force decreases weakly with γ, whereas the buckling compression is almost constant over the whole γ-range (Fig. 6). The behavior for compressions after rotation is the same as in the TS geometry.

For a vesicle lying on its face compressed by a large sphere (the FL geometry), shown in the bottom row of Fig. 7, the progressive confinement involves a global deformation of the vesicle even for small compressions. In this case the contact area between vesicle and sphere is much larger than for the other two geometries. Moreover, compression directly results in deformation of all the ''vertical'' ridges. For $\gamma < 130$, the vesicles rotate upon compression but no buckling is observed for compressions up to 50%. For $150 < \gamma < 5 \times 10^3$, we find simultaneous rotation and buckling of the upper and lower tip, as illustrated in the bottom row of Fig. 7 and shown in Supplementary Material, Movie S1. For $5 \times 10^3 < \gamma < 10^5$, the buckling transition occurs between two asymmetrically deformed states, but a rotation occurs only at larger compressions. Finally, for $\gamma > 10^5$, buckling is replaced by crumpling, as discussed above for the TS geometry.

For the FL and FS geometries, we also performed simulations for vesicles that were ''glued'' with one face to the substrate to prevent rotation. In these cases, we found qualitatively similar buckling behavior. The deformation process for a glued shell of $T = 48$ and $\gamma = 1000$ is shown in Movie S2. The main difference with the rotating shells is that the threefold rotational symmetry of the deformed state before and after the buckling transition is now clearly broken. In the FS geometry, the vesicle deforms asymmetrically in such a way that one of the corners of the top face touches the confining sphere, see middle row of Fig. 7. In the FL geometry, the buckling behavior for small γ is different, as the buckling force is now almost independent of γ for $\gamma < 5 \times 10^3$ (compare Fig. 6), whereas the large-γ behavior remains unchanged.

Measuring elastic parameters

The simulation results presented here show that a rough estimate of the product $K_0\kappa$ of elastic constants can be obtained straightforwardly from force-compression measurements. The next question is how to determine K_0 and κ separately. In a study by Ivanovska et al. (20), the elastic parameters of viral capsids were estimated by employing elasticity theory for a thin shell of a homogeneous material with three-dimensional Young modulus Y and thickness equal to the size of the protein subunits.

We propose instead to fit the experimental virus shape to the theoretical predictions in the relaxed state to determine γ, as done in Lidmar et al. (24). This gives information on the ratio K_0/κ. With this information, $K_0\kappa$ can be extracted precisely from force-compression measurements.

Alternatively, force-compression experiments alone can be used to extract K_0 and κ. This can be done either in the FL- or the TS-geometry. Since it may be difficult experimentally to balance a virus or vesicle on its tip, we focus on the FL-geometry. In this case, the γ-value can be determined from the curve of buckling compressions shown in Fig. 6 *B*. From the experimentally measured buckling compression between two plates, $\Delta z/2R_v$ can be calculated and used to read off the value of γ in Fig. 6 *B*. With this information, the curve of the buckling force in Fig. 6 *A* can be used to obtain $K_0\kappa$.

SUMMARY AND DISCUSSION

We have employed a discrete bead-spring model to study the elastic deformation of viral capsids and crystalline vesicles. Simulations indicate that there are two globally different force-deformation scenarios for confined vesicles with icosahedral symmetry. In the first case, for small γ, there is a linear dependence of the force on the compression. In the second case the vesicle undergoes a buckling transition in which one or two of the tips of the icosahedron buckle inward. The detailed buckling pathway depends on the confining geometry.

A linear force-deflection dependence has been measured experimentally for the bacteriophage $\phi 29$ by Ivanovska et al. (20) to a maximum compression between 15 and 20%. For the $T = 3$ shell we do find a large linear regime for either $\gamma < 100$ with a slope $5 < C_\alpha < 9$ depending on the exact value of γ, or for small sphere radii $R_s/R_v < 0.5$. In all cases, the buckling compression is ~25%. For a triangulation with a larger T-number of $T = 192$, a linear regime up to 20% compression with a slope $5.5 < C_\alpha < 6.5$ exists for $\gamma \leq 250$. It should be noticed, however, that $\phi 29$ is not an icosahedral virus (as discussed in the Introduction), so a detailed quantitative comparison is not possible. We conclude that $\phi 29$ is characterized by a small Föppl-von Kármán number, in agreement with the results for other small viruses like the yeast L-A virus (24).

Our data indicate that there are strong finite-size effects in our model for small viruses. This raises the question about the correspondence of the mesh points of the triangulated surface model with the protein structure of viral capsids. In Zandi et al. (14), self-assembly has been described successfully by a model, which is equivalent to identifying capsomers with vertices, i.e., a $T = 3$ virus is modeled by a $T = 3$ triangulated surface. On the other hand, a continuum description has been shown in Lidmar et al. (24) to reproduce very well the shape of viral capsids. This corresponds to the assumption that the protein subunits are themselves flexible, and interact sufficiently strongly that the capsid behaves like a thin shell of a uniform isotropic elastic material. We believe that the correct description must lie somewhere between these two limiting cases. Atomistic simulations might be able to provide the required information about the elasticity of protein subunits and their interactions.

SUPPLEMENTARY MATERIAL

An online supplement to this article can be found by visiting BJ Online at http://www.biophysj.org.

The authors thank Paul van der Schoot, Willem Kegel and Alex Evilevitch for inspirational discussions.

REFERENCES

1. Hubert, H., B. Devouard, L. A. J. Garvie, M. O'Keeffe, P. R. Buseck, W. T. Petuskey, and P. F. McMillan. 1998. Icosahedral packing of B12 icosahedra in boron suboxide (B6O). *Nature*. 391: 376–378.
2. Dubois, M., B. Demé, T. Gulik-Krzywicki, J.-C. Dedieu, C. Vautrin, S. Désert, E. Perez, and T. Zemb. 2001. Self-assembly of regular hollow icosahedra in salt-free catanionic solutions. *Nature*. 411: 672–675.
3. Liu, T., E. Diemann, H. Li, A. W. M. Dress, and A. Müller. 2003. Self-assembly in aqueous solution of wheel-shaped Mo_{154} oxide clusters into vesicles. *Nature*. 426:59–62.
4. Shepherd, C. M., I. A. Borelli, G. Lander, P. Natarajan, V. Siddavanahalli, C. Bajaj, J. E. Johnson, C. L. Brooks III, and V. S. Reddy. 2006. VIPERdb: a relational database for structural viruses. *Nucleic Acids Res*. 34:D386–D389.
5. Caspar, D. L. D. 1956. Structure of small viruses: tomato bushy stunt virus. *Nature*. 177:475–476.
6. Harrison, S., A. Olson, C. Schutt, F. Winkler, and G. Bricogne. 1978. Tomato bushy stunt virus at 2.9 Å resolution. *Nature*. 276:368–373.
7. Tao, Y., N. H. Olson, W. Xu, D. L. Anderson, M. G. Rossmann, and T. S. Baker. 1998. Assembly of a tailed bacterial virus and its genome release studied in three dimensions. *Cell*. 95:431–437.
8. Smith, D. E., S. J. Tans, S. B. Smith, S. Grimes, D. L. Anderson, and C. Bustamante. 2001. The bacteriophage straight $\phi 29$ portal motor can package DNA against a large internal force. *Nature*. 413: 748–752.
9. Evilevitch, A., L. Lavelle, C. M. Knobler, E. Raspaud, and W. M. Gelbart. 2003. Osmotic pressure inhibition of DNA ejection from phage. *Proc. Natl. Acad. Sci. USA*. 100:9292–9295.
10. Ceres, P., and A. Skolnick. 2002. Weak protein-protein interactions are sufficient to drive assembly of hepatitis B virus capsids. *Biochemistry*. 41:11525–11531.
11. Kegel, W. K., and P. van der Schoot. 2004. Competing hydrophobic and screened-Coulomb interactions in hepatitus B virus capsid assembly. *Biophys. J*. 86:3905–3913.
12. van der Schoot, P., and R. F. Bruinsma. 2005. Electrostatics and the assembly of an RNA virus. *Phys. Rev. E*. 71:061928.
13. Bruinsma, R. F., W. M. Gelbart, D. Reguera, J. Rudnick, and R. Zandi. 2003. Viral self-assembly as a thermodynamic process. *Phys. Rev. Lett*. 90:248101.
14. Zandi, R., D. Reguera, R. F. Bruinsma, W. M. Gelbart, and J. Rudnick. 2004. Origin of icosahedral symmetry in viruses. *Proc. Natl. Acad. Sci. USA*. 101:15556–15560.
15. Rapaport, D. C. 2004. Self-assembly of polyhedral shells: a molecular dynamics study. *Phys. Rev. E*. 70:051905.
16. Nguyen, T. T., R. F. Bruinsma, and W. M. Gelbart. 2005. Elasticity theory and shape transitions of viral shells. *Phys. Rev. E*. 72:051923.
17. Coxeter, H. M. S. 1969. Introduction to Geometry. Wiley, New York.
18. Caspar, D. L. D., and A. Klug. 1962. Physical principles in the construction of regular viruses. *Cold Spring Harb. Symp. Quant. Biol*. 27:1–50.
19. Reddy, V. S., H. A. Giesing, R. T. Morton, A. Kumar, C. B. Post, C. L. Brooks III, and J. E. Johnson. 1998. Energetics of quasiequivalence: computational analysis of protein-protein interactions in icosahedral viruses. *Biophys. J*. 74:546–558.
20. Ivanovska, I. L., P. J. de Pablo, B. Ibarra, G. Sgalari, F. C. MacKintosh, J. L. Carrascosa, C. F. Schmidt, and G. J. L. Wuite. 2004. Bacteriophage capsids: tough nanoshells with complex elastic properties. *Proc. Natl. Acad. Sci. USA*. 101:7600–7605.
21. Caruso, F., R. A. Caruso, and H. Möhwald. 1998. Nanoengineering of inorganic and hybrid hollow spheres by colloidal templating. *Science*. 282:1111–1114.
22. Lulevich, V. V., D. Andrienko, and O. I. Vinogradova. 2004. Elasticity of polyelectrolyte multilayer microcapsules. *Langmuir*. 120:3822–3826.

23. Fery, A., F. Dubreuil, and H. Möhwald. 2004. Mechanics of artificial microcapsules. *N. J. Phys.* 6:1–13.
24. Lidmar, J., L. Mirny, and D. R. Nelson. 2003. Virus shapes and buckling transitions in spherical shells. *Phys. Rev. E.* 68:051910.
25. Seung, H. S., and D. R. Nelson. 1988. Defects in flexible membranes with crystalline order. *Phys. Rev. A.* 38:1005–1018.
26. Lobkovsky, A. E., S. Gentes, H. Li, D. Morse, and T. A. Witten. 1995. Scaling properties of stretching ridges in a crumpled elastic sheet. *Science.* 270:1482–1485.
27. Zhang, Z., H. T. Davis, R. S. Maier, and D. M. Kroll. 1995. Asymptotic shape of elastic networks. *Phys. Rev. B.* 52:5404–5413.
28. Bustamante, C., Z. Bryant, and S. B. Smith. 2003. Ten years of tension: single-molecule DNA mechanics. *Nature.* 421:423–427.
29. van Gunsteren, W. F., and H. J. C. Berendsen. 1982. Algorithms for Brownian dynamics. *Mol. Phys.* 45:637–647.
30. Landau, L. D., and E. M. Lifshitz. 1986. Theory of Elasticity. Butterworth-Heinemann, Boston.
31. DiDonna, B. A., and T. A. Witten. 2001. Anomalous strength of membranes with elastic ridges. *Phys. Rev. Lett.* 87:206105.
32. DiDonna, B. A. 2002. Scaling of the buckling transition of ridges in thin sheets. *Phys. Rev. E.* 66:016601.
33. Hertz, H. 1882. Über die berührung fester körper. *J. Reine Angew. Mathematik.* 92:156–171.